

# Real-Time Detection of Unmodeled Gravitational-Wave Transients Using Convolutional Neural Networks

Vasileios Skliris, Michael R. K. Norman, and Patrick J. Sutton

*Gravity Exploration Institute, School of Physics and Astronomy,  
Cardiff University, Cardiff, United Kingdom CF24 3AA*

(Dated: November 1, 2021)

Convolutional Neural Networks (CNNs) have demonstrated potential for the real-time analysis of data from gravitational-wave detector networks for the specific case of signals from coalescing compact-object binaries such as black-hole binaries. Unfortunately, training these CNNs requires a precise model of the target signal; they are therefore not applicable to a wide class of potential gravitational-wave sources, such as core-collapse supernovae and long gamma-ray bursts, where unknown physics or computational limitations prevent the development of comprehensive signal models. We demonstrate for the first time a CNN with the ability to detect generic signals – those without a precise model – with sensitivity across a wide parameter space. Our CNN has a novel structure that uses not only the network strain data but also the Pearson cross-correlation between detectors to distinguish correlated gravitational-wave signals from uncorrelated noise transients. We demonstrate the efficacy of our CNN using data from the second LIGO-Virgo observing run. We show that it has sensitivity approaching that of the “gold-standard” unmodeled transient searches currently used by LIGO-Virgo, at extremely low (order of 1 second) latency and using only a fraction of the computing power required by existing searches, allowing our models the possibility of true real-time detection of gravitational-wave transients associated with gamma-ray bursts, core-collapse supernovae, and other relativistic astrophysical phenomena.

## I. INTRODUCTION

Gravitational-wave (GW) astronomy is now an established field of observational science. To date, the LIGO [1] and VIRGO[2] collaborations have published the details of 15 high-confidence detections [3–7], and released public alerts for more than 50 additional candidate signals [8]. The detected signals originate from the binary inspiral and merger of two black holes [9], two neutron stars [10], or one object of each type [11].

Low-latency detection of candidate signals offers arguably the greatest potential scientific payoff, as the GW observations can trigger followup observations in other channels; *i.e.*, multi-messenger astronomy. For example, combined GW and electromagnetic observations of GW170817 - GRB 170817A [12] have yielded novel insights into the origin of heavy elements [13], neutron-star structure [14], GRB astrophysics and host environments [15], and the Hubble constant [16]. Electromagnetic followup of gravitational-wave signals requires very low latency analysis of the GW data - preferably at the second scale to capture the highest energy emissions (*e.g.*, the prompt gamma and x-ray emission of GRBs), so that it produces accurate sky localisation results to make the follow up possible. Current low-latency GW analysis techniques rely on hundreds of dedicated CPUs and achieve minute-scale latency for automated alerts [17].

Recent work by a number of authors [18–22] has shown that a fundamentally different approach using convolutional neural networks (CNNs) has the potential to analyse detector data for GW signals in real time ( $\sim 1$  s latency) using a single dedicated GPU. However, CNNs demonstrated to date are only capable of detecting signals with a precisely defined signal model (*i.e.*, compact

binary coalescences) that is used to train the network. Many potential sources are governed by physics which is either unknown (*e.g.* the neutron star equation of state) [23] and/or computationally intractable (*e.g.* the modelling of core-collapse supernovae [24] and accretion-disk instabilities [25]); their transient signals are commonly known as gravitational wave bursts (GWBs). While the unknown physics governing GWBs makes the study of such signals exciting, it also poses a challenge: to fully explore the new GW window we need to be able to detect signals from the widest possible variety of sources without relying on precise models for training.

We address this challenge by proposing a novel CNN architecture that analyses not only the detector strain data directly but also the cross-correlation timeseries between detectors. By training the CNN with ‘featureless’ randomised signals, we are able to construct a neural network that detects coherence (amplitude and phase consistency) between detectors rather than specific signal shapes in individual detectors. We test the trained CNN with real data from the LIGO-Virgo network and show that it is capable of detecting a variety of simulated GWB signal morphologies without being specifically trained for them, at sensitivities close to that of standard GWB searches, but at much lower latency and a tiny fraction of the computational cost.

This paper is organised as follows. In Section II we give a brief review of applications of machine learning in gravitational-wave astronomy. In section III we present the architecture of our CNN and describe the analysis and training procedures. In Section IV we present the performance of the trained CNN on both simulated and real LIGO-Virgo data. We discuss the implications of these results and next steps in Section V.

## II. MACHINE LEARNING IN GRAVITATIONAL-WAVE ASTRONOMY

The fields of gravitational-wave astronomy and deep learning have both advanced significantly in recent years. As such, there has been a confluence of research into their combination and a considerable body of work has developed. Artificial neural networks, including CNNs, autoencoders [26], and various other architectures, have been applied to a variety of problems within gravitational-wave astronomy. First among these was the detection of signals from the merger of compact binaries of black holes and/or neutron stars [18–21, 27–33]. Parameter estimation [22, 27, 31, 34], and denoising [26, 32, 35] have been a significant area of interest; as well as detector glitch classification [36, 37], and waveform modeling.

There has been somewhat less interest in the application of deep learning to the detection of other, as yet undetected, gravitational-wave sources, although there have been a number of studies into the efficacy of using ANNs to detect supernovae waveforms [38, 39]. This has been made possible primarily through a number of recent attempts to produce supernovae gravitational-wave templates through multidimensional simulation [40–43]. However it should be noted that some of these utilise approximations as the required physics is much less understood than in the CBC case.

There are two natural ways to input the data into CNN models, as 1D time series or as 2D time-frequency maps. The most obvious is to input the 1D time series - this preserves the full data output of the detectors. A 2019 paper by Chan et al. [44] applied convolutional neural networks to simulated gravitational wave time series with core collapse supernovae injections. They used a deep convolutional network consisting of 8 convolutional layers and 3 dense layers, and input all four gravitational wave detectors of the LIGO-VIRGO-Kagra network as well as all four with the two LIGO detectors in Advanced LIGO configurations. Their False Alarm Probability was set at 10% a much higher false alarm rate than is being presented here, and focused only on supernovae waveforms. They tested four different supernovae waveforms, notably not included in the training bank, and achieved accuracies between 53% and 90%.

The second method, inputting the data as 2D time-frequency maps, is closer to the most successful domain of CNNs: image recognition. There have been several papers which investigate this method's application to supernovae. A 2020 paper by Iess et al. [39] investigates the application of CNNs to both 1D gravitational wave time-series and 2D time-frequency plots of simulated Virgo and Einstein telescope noise with injected simulations of neutrino-driven core-collapse supernovae. They also attempt to account for transient glitches by including training examples with injected sine-Gaussian's and approximated representations of scattered light glitches. They achieve a single detector accuracy of over 95% for both

1D and 2D CNN pipelines. Instead of running the CNN across all data they use a Wavelet detection filter to generate triggers and a value for the SNR.

2D time-frequency maps can also be inputted in multi-detector configurations, similar to the 1D case. Each detector can be added to the depth channel in a similar way to how the RGB channels are usually handled in generic image classification. An example of this can be seen in a 2018 paper by Astone et al. [38] wherein a CNN is used to classify multi-channel time-frequency images of the two LIGO detectors and the Virgo detector. Rather than using a hydro-dynamically simulated template bank, they opt for a engineered waveform which can replicate many of the features seen in simulated waveforms - this allows for a larger exploration of possible parameter space. They measured results at a FAR of  $7 \times 10^{-5}$  Hz With efficiencies above 90% at an SNR of 20. A 2020 paper by Lopez et al. [45] introduces a complex mini-inception resnet neural network to detect waveforms found in time-frequency images of 3D simulations of core collapse supernovae. Again three detectors were used with each detector layered as depth in the time frequency image. They achieved a detection efficiency of 70% at a False Alarm rate of 5%, on signals injected into real noise data from O2.

A 2020 paper by Marianer et al. [46] also utilises 2D time-frequency maps, however their method is considerably different to most others mentioned here, rather than searching only for coherence they employ an anomaly-detection method to search for anomalous features. A CNN was trained on the Gravity Spy glitch dataset [47], then two distinct methods of outlier detection were applied to the the CNN. This search was applied to a significant subset of public LIGO data from the first two observing runs with no promising candidates.

Our method competes with the search by Marianer et al. Aside from their search method, which differs significantly for the method discussed in this paper, all previous studies have relied on constrained template banks to detect specific phenomenon and have not attempted a generalised gravitational-wave detection method.

The detection technique presented by the rest of this paper utilises two distinct CNN models combined in ensemble to produce a single output score. One model looks for any coincident signals and the other verifies that these are coherent.

## III. A CNN FOR UNMODELLED BURST DETECTION

### A. Network Architecture

Our goal is to be able to detect sub-second-duration GWBs in data from the three detectors of the LIGO-Virgo network, without prior knowledge of the signal morphology. A significant challenge is to distinguish real signals from the background noise transients, “glitches”,

that are common in these detectors [48–50]. Typical GWB detection algorithms [51–54] do this by requiring candidate signals to be seen simultaneously in multiple detectors (simultaneously up to the light travel time between the detectors) and to be correlated between detectors. We follow this logic in our analysis by using a network architecture that combines the outputs of two different CNNs: one that detects coincident signals in multiple detectors (Coincidence model - Model 1), and a second that detects correlation in phase and amplitude between the detectors (Coherence model - Model 2).

### 1. Coincidence Model - Model 1

The first CNN is a single-input single-output residual neural network whose main goal is to identify real signals from noise. More specifically it tries to identify coincident signals that appear in at least two detectors. This model takes as input the whitened timeseries data from each of the three LIGO-Virgo detectors. The output is a score on  $[0, 1]$ , where high values indicate signal and low values no signal.

Residual neural networks are proven to boost the performance of simpler CNNs by reducing the effect of vanishing gradients; the latter make deep CNNs loose contributions from their first layers and cause their efficiency to saturate. We adapt a network from [55] and optimise it using a genetic algorithm (see below). We find that the resulting residual neural networks outperforms “ordinary” deep CNNs in our case.

More specifically we optimised the residual blocks and we tried to find the simplest CNN model with a relatively good performance (overall accuracy  $> 95\%$ ) to use as our residual block. To find the hyper-parameters of the model we used a genetic algorithm, designed by Michael Norman, that trained many generations of different randomly initialised models and found which hyper-parameters seem to increase the performance. The main two differences from the original model of [55] was the kernel size that is quite bigger in our application and the reduction one layer from three layers to two in the residual blocks. We also tried to see how many residual blocks are optimal and we saw that three are enough, as it is in the original model. Filter size variations had not obvious effect on the performance and we chose to follow the original sizes on this to make the model less computationally expensive. The final addition was the use for cyclical learning rate [56] that boosted our performance by 2%.

This residual network as you can see in figure 1 has three residual blocks. The first has filter size of 64 and the last two 128. At the end of each residual block we add the the filters of the first layer of that block to the output. By doing this the gradient can skip the intermediate layer reducing the vanishing effect. Due to the fact that we use convolution, all layers are zero-padded to maintain the same size with the input and make this ad-

dition feasible. At the end of each layer we apply ReLU activation followed by batch-normalisation.

Finally after the last residual block we flatten all the parameters using global average pooling. Following that we used two fully connected layers with batch-normalisation before get to the output. The output layer has a sigmoid activation and for the calculation of the loss we used binary cross entropy.

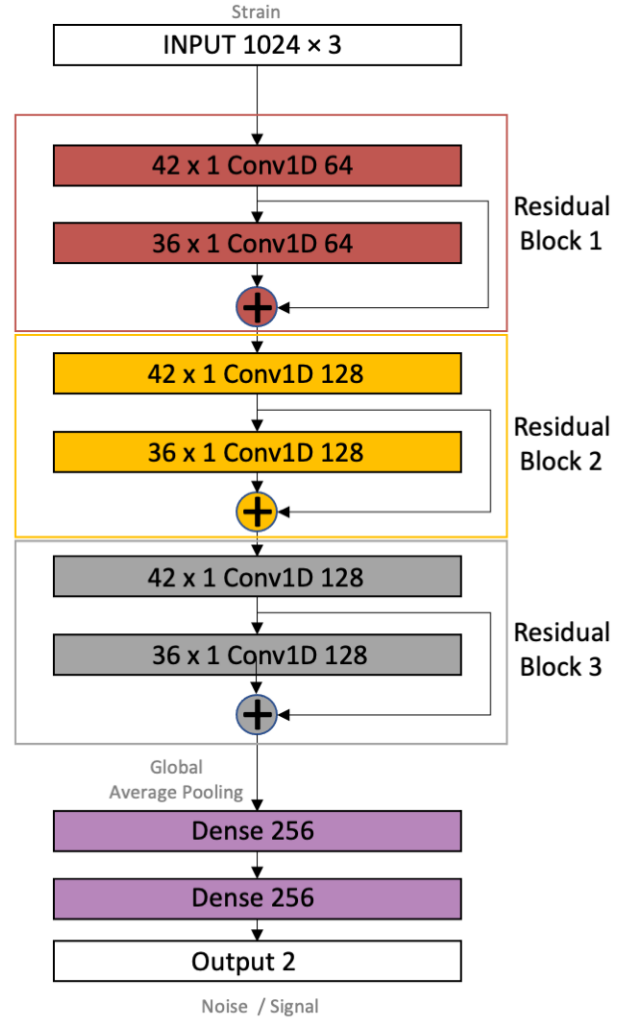


Figure 1: Coincidence model architecture

As we discussed before this model searches for signals that are present to at lease two detectors. We trained with simulated noise, signals and glitches with in proportions appropriate to focus on that goal. We discuss this more in the training methods III C 2

### 2. Coherency Model - Model 2

The second model has two inputs and one output. The first input is the same whitened timeseries data fed to the first model, while the second input is the Pearson correlation of each pair of detectors. We have attempted to train

networks to understand the correlation information from the strain data. Although after a lot of experimentation there was no clear evidence that this is feasible and for burst detection correlation information is crucial to reach low false alarm rates. Furthermore, even if this was possible, it is an unnecessary computational burden as the Pearson correlation is simple to compute and more easy to digest by a feature detecting algorithm. Evidently we decided to feed the correlation as an input.

$$r_{\alpha\beta}[n] = \frac{\sum_{i=1}^N (d_\alpha[i] - \bar{d}_\alpha)(d_\beta[i+n] - \bar{d}_\beta)}{\sqrt{\sum_{j=1}^N (d_\alpha[j] - \bar{d}_\alpha)^2 \sum_{k=1}^N (d_\beta[k] - \bar{d}_\beta)^2}}. \quad (1)$$

Here  $d_\alpha[i]$  is the whitened data timeseries for detector  $\alpha$ ,  $\bar{d}_\alpha$  is the mean over  $N$  samples, and  $n$  is an integer time delay between detectors. The correlation is computed for all  $n$  corresponding to time delays of up to  $\pm 30$  ms in respect to the first detector. This is the maximum arrival time delay a signal can have between the three detector network.

These two inputs have their own separate branches and eventually merge their features in one as you can see in Figure 2.

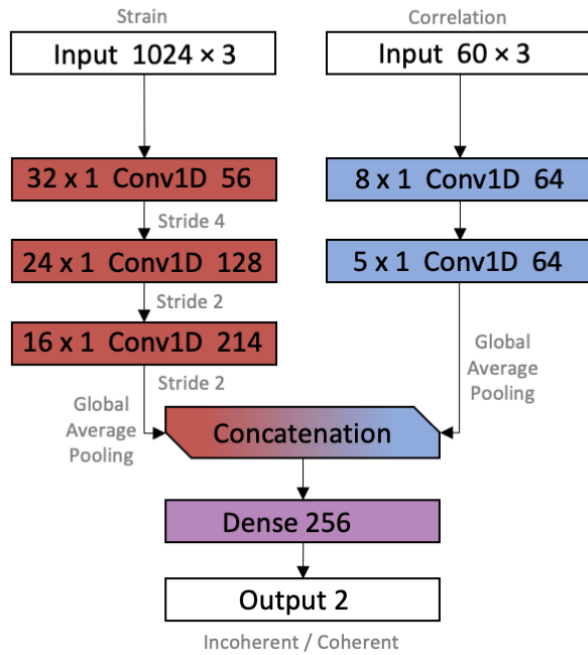


Figure 2: Coincidence model architecture

Due to the small size of the input the network didn't need to be as deep as the coincidence model. We also used a genetic algorithm, designed by Michael Norman, to figure out which hyper-parameters work better. An interesting observation was that in this model the number of filters is a sensitive parameter that can prevent the model from training at all if it increased or decreased at

any of the convolutional layers. On the contrary, variations on the kernel size had surprisingly no big effect on performance, except some variations on the stability of training in some cases. The choice for kernel size was made based on how often those numbers appeared in the gene pool of last generation of successful models.

There has been an attempt to use residual neural network for the "Strain" branch of the model but is seemed to be an unnecessary complication because the performance is the same. That shouldn't surprise us because the problem that the model is trying to address is different. The two branches of the coherency model are flattened using global average pooling which as in model 1 showed to increase the performance slightly.

This model has also a binary classification output that returns a measure of coherency among any detectors [0,1]. To achieve that we use a different group of datasets than the coincidence model. We use simulated noise and signals but also a combination of coincident and not coincident uncorrelated signals.

## B. Analysis Procedure

In our analysis we use two types of background noise. The one we use for training is Gaussian noise that follows the design curve for the LIGO detectors [57]. For testing we use publicly available data from the LIGO-Virgo detectors. They are read from files accessible from the GW open science center (GWOSC)[58] (<https://www.gw-openscience.org/O2/>). Important mention again that real detector noise is used only for testing and not for training. The three detectors are denoted H (Hanford), L (Livingston), and V (Virgo). The power spectral density  $S_\alpha(f)$  for each detector  $\alpha$  is computed using Welch's method, and used to whiten the corresponding data stream. The Pearson correlation is computed between each pair of detectors. The bandpassed [20,512]Hz - whitened data series and the correlation series are then fed into the two models. Finally, the scores from the two models are multiplied together to give a combined score on [0, 1]. In this way a candidate signal needs to score highly for both models; *i.e.*, showing both coincidence in multiple detectors and correlation between the detectors.

The LIGO-Virgo data used, from GWOSC[58], were sampled at 4096 Hz. We downsample to 1024 Hz, allowing us to detect signals up to 512 Hz; this covers the most sensitive frequency range of the detectors and is sufficient for the purpose of demonstrating our CNN. (Since the trained network can process data much faster than real time, we can easily extend the analysis to higher sample rates.) We chose to focus on signal durations  $< 1$  s by analysing data in 1 s segments. This covers many plausible signal models, including for example core collapse supernovae [24], perturbed neutron stars and black holes [11], and cosmic string cusps [59]. We can easily extend to longer durations as well (with a corresponding increase in latency). At our chosen sampling rate this means that

the timeseries data is fed to the CNN in an array of size [1024 x 3]. The Pearson correlation is computed for time delays in steps of one sample over  $\pm 30$  ms, for a total of 60 samples; this data is therefore in an array of size [60 x 3]. We use H as the reference and apply the time delays to the L and V timeseries.

To estimate the distribution of scores of the background noise, we repeat the analysis many times after time-shifting the data between detectors by an integer number of seconds. Since the time shift is much larger than the largest possible time-of-light delay between detectors, it prevents a real GW signal from appearing in coincidence between multiple detectors. All coincident events in the time-shifted series can therefore be assumed to be uncorrelated and treated as background noise. This is a standard procedure in GW analysis; see *e.g.* [48].

To estimate the sensitivity to GWBs, we repeat the analysis after adding simulated signals to the data. In General Relativity, a GW has two polarisations, denoted  $h_+(t)$  and  $h_\times(t)$ . The received signal  $h_\alpha(t)$  of a given detector  $\alpha$  is the combination

$$h_\alpha(t) = F_\alpha^+ h_+(t) + F_\alpha^\times h_\times(t) \quad (2)$$

where the antenna response functions  $F_\alpha^{+,\times}$  are determined by the position and orientation of the source relative to the detector. We characterise the strength of the received signal by its network signal-to-noise ratio

$$\rho = \sqrt{\sum_\alpha 4 \int_0^\infty \frac{|\tilde{h}_\alpha(f)|^2}{S_\alpha(f)} df}. \quad (3)$$

Generating simulated signals distributed isotropically over the sky and rescaling to different  $\rho$  values allows us to measure the distribution of CNN scores as a function of the signal-to-noise ratio of the signal.

### C. Training

The choice of data used to train a CNN is a critical factor for the CNN's performance.

For the signal population we use white-noise bursts (WNBs) [48, 53]; these are signals where the  $h_+$  and  $h_\times$  polarisations are independent timeseries of Gaussian noise that is white over a specified frequency range, multiplied by a sigmoid envelope. We select these as our training sample as they are effectively featureless. The bandwidth of each injection is selected randomly and uniformly over the range [40, 480] Hz. The duration of each injection, is selected randomly and uniformly over the range [0.05, 0.9] s. Given their duration their central time is positioned randomly inside this 1 second interval in a way that they don't get cropped. The injections are distributed uniformly over the sky and projected onto the detectors using equation (2). Finally, the signal is rescaled to a desired network signal-to-noise ratio  $\rho$  as defined in equation (3). In the rest of this section we will

discuss different aspects of our training data and methods, that eventually gave us the current best model.

#### 1. Code

All training data was generated using the MLY-pipeline package [60] and its generator function, with elements of the PyCBC [61] and GWPY[62] package to project the signal onto the detectors and apply time-of-flight differences to the signals arriving at the various detector locations. For training the models we used KERAS [63]. More details and the codes are available at our repository [64].

#### 2. Data types

Each model is trained with different datasets that focus on challenging the models to archive their best performance on each of their tasks. All data instances have background noise and if applicable a type of injection. For the background samples, we find in practice that the best CNN performance is obtained by training with *simulated* detector noise and glitches, rather than real glitchy detector noise. We therefore use Gaussian noise with a power spectrum that follows the design curve for the LIGO detectors [57] to model the stationary component of the LIGO-Virgo background noise. The reason the performance is better is that by using real noise the frequency of glitches is not enough for the model to learn to recognise them. In our application we created noise instances with glitches and we can control the frequency they appear. As it will be shown later this helps a lot with the reduction of false alarms.

For the coincidence model we use three types of data instances: noise, glitches and signals. Noise follows the stationary component of LIGO-Virgo background with addition of random fluctuations. To simulate these fluctuations we generate white Gaussian noise in the frequency domain (real and imaginary parts are generated independently as Gaussian distributed random numbers). Then the noise value in each frequency bit  $k$  is multiplied by  $\sqrt{S[k]}$  where  $S$  is the PSD of the theoretical curves. For every generation of noise we do this process to create different instances of the same type of noise. For the glitches we use the same waveform bank as we do with signals but for each instance we do the injection to a randomly chosen detector. Those injections will have a variety of SNR values [6,70]. Noise and glitch datasets are both labeled as "noise", they belong in the same classification class. Signals are the only type labeled as "signal" and they are injected in all three detectors as described above with SNR values inside the range [12,30]. The limits of this range are chosen based on the fact that lower SNR values in training increase the false alarm rates dramatically and that higher SNR than 30 is quite obvious to be detected by the simplest pipeline and as proven

later the detection efficiency holds to higher SNR values than trained ones.

For the coherency model we use also three types of data. Noise and signals are as before with the difference that the range of SNR values now is [10,50]. The third type are the incoherent signals. This type is also labeled as "noise" and they represent the extreme cases where glitches or non gaussianities are present in at least two detectors. To make this we randomly select three different injections from our bank and we inject them in the detectors like they are three projections of same signal. Their network SNR is in the range [10,70]. There are three subcategories of this type that are themselves three extra datasets.

Pearson correlation is calculated only around the window of  $\pm 30s$ . We expect that even different signals will have some kind of excess correlation, although this correlation will not be the same in all three pairs of detectors (HL,HV,LV). Moreover each injection can have different duration which will affect the overlap of those signals.

To control that we created a metric called "disposition". Disposition is the range the central times of those signals. In the case of three detectors and a disposition of 0.5 seconds one randomly selected signal will be put on 0 seconds the next on 0.25 seconds and the last one on 0.5 seconds. All together will be randomly positioned in the 1 second interval so that no signal gets cropped. Finally given the disposition there is a restriction imposed on the injection duration. The maximum duration allowed for a selected injection is practically 1 second - disposition. We generate three datasets with disposition options. The first one has range of [100,500] (3a) milliseconds, the second [0,100] (3b) and the last one has zero disposition (3c) to challenge the model with coincident incoherent signals.

The list below summarises all the types of data we used:

- **Type 1:** Gaussian LIGO-Virgo noise, with no injections. Labeled as noise.
- **Type 2:** Gaussian LIGO-Virgo noise with coherent WNB injections in all detectors, simulating a real GWB. Labeled as signal.
- **Type 3:** Gaussian LIGO-Virgo noise with different (incoherent) WNB injections in each detector, simulating unrelated glitches or excess noise in each detector. The injections may be simultaneous or offset in time from each other to simulate simultaneous or nearly simultaneous glitches. Labeled as noise.
- **Type 4:** Gaussian LIGO-Virgo noise with a single WNB injection in a randomly chosen detector, simulating a glitch in a single detector. Labeled as noise.

### 3. Reproducibility

It is crucial for one method or model to have reproducible results if it is going to be compared with another. Machine learning models usually have random initialisation of their trainable parameters, which can lead to different results. To address this effect we train a given model multiple times to see how important is this effect and most importantly the variance of the results. This is important for the next subsections where we compare different methods of training.

The variation is present on the false alarm rate test and the efficiency curve (see section IV). For the false alarm rate what varies is the score of the loud events. For the efficiency the variation depends on how sensitive is the model to a signal but it also depends on the the loudest false alarm rate event because it defines the threshold above which we define a detection.

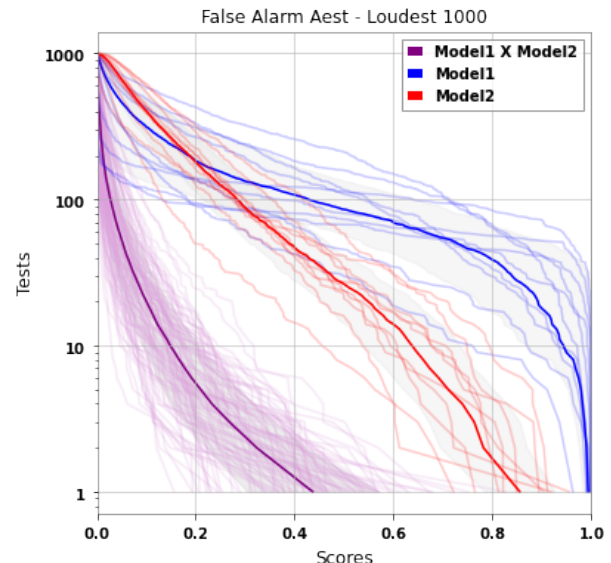


Figure 3: False alarm rate curves of 10 identical coincident models (blue) and 10 identical coherent models (red). The 100 combinations of model 1 and 2 are shown in purple. The highlighted lines are the mean false alarm rate curves for each case. The variance of the results is shown in light gray. Only the 1000 loudest events in a month for each model are shown here

In figure 3, we trained a pair of models 1 and 2, ten times each. This provides a good enough estimation of the variance and mean of the false alarm curve. Additionally by combining all the possible pairs we get 100 independent tests of the final model. This practice is followed in the next subsections where we compare the same models under different methods of training.

#### 4. Input ratios

In more common classification problems the training data have the same amount of examples in each case, because all classes are equal and there is not preference in the performance. In this problem we prioritise the reduction of false alarms (false positives) and the ability of the network to understand how noise looks like, instead of what is a signal. Even with our best model, a 50-50 ratio gives back a false alarm rate of 1/day. Furthermore we have more than just simple noise and injection in our data types, and we try to simulate a real noisy detector with Gaussian noise and WNBs, so we also needed to investigate what are the optimal proportions of each type. We trained both models with different ratios of the their data types to check which one provides the best performance.

For model 1 we tried 12 different proportions of training data. We tested combinations of data size of Type 2, 4 and 1 with choices being (3,6), (3,6,12) and (3,6) respectively of  $10^4$  instances. For model 2 we tried 16 different combinations, of Type 2, 3a & b together, 3c and 1 with choices being (5,10)  $10^4$  for each of them. For all those different proportions we train 7 models and we use the mean false alarm curve and efficiency test for comparisons. We get in total  $12 \times 16 = 192$  different combinations of model 1 & 2. As it is described in more detail in section IV, the ranking of a model is defined by the 50% threshold of its efficiency on a fixed false alarm rate. After training, all models were tested for false alarms with the exactly same background noise from O2 LIGO-Virgo scientific run during August 2017. Additionally we run an efficiency test on various waveform types to all models, using again the same exact background data and injections for all models so that the comparison is robust.

The combination of proportions with the best performance from each type is the one that follows 3-6-3 (Type 2 - Type 4 - Type 1) proportion for model 1 and 5-10-5-5 (Type 2 - Type 3a&b - Type 3c - Type 1) for model 2. In both cases it is interesting to see that for the best training we need much more glitch like data than plain noise or signals. That supports the idea that real noise cannot provide the best training data.

#### 5. Elevated Virgo

As it is stated before we train with artificial Gaussian noise the follows the PSD of the advanced LIGO and Virgo detectors. Although that PSD is not a perfect representation of the real data noise level, because the noise is not advanced LIGO-Virgo level yet. More specifically, the artificial Virgo level of noise is much lower than what is in the real detectors. For that reason we experimented on training the best model from the previous investigation (IIC 4) with different noise elevation for Virgo, by multiplying with powers of two: [0.5,1,2,4,8,16,32]. The

case of 1 is the same models from before and the case of 0.5 is for a sanity check on the method. All other multipliers were tried to see how the models will behave. Again for each model we did 7 different training case and used the mean to compare the different multiplier methods.

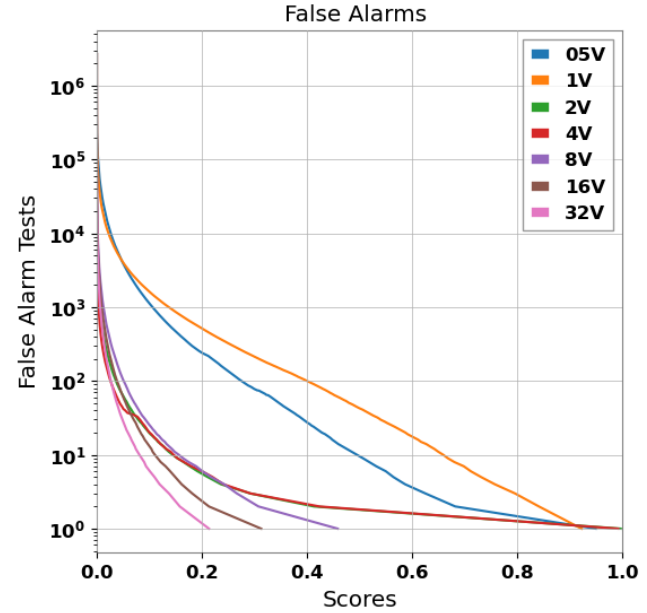


Figure 4: Average false alarms (out of 49 different combinations of model 1 and model 2) of different Virgo elevations (1/month).

As you can see in figure 4 the higher the elevation the better the false alarm rate. That is expected because if Virgo is much louder than LIGO detectors most of the SNR contribution will go to Hanford and Livingston strains. Eventually a lower false alarm threshold, makes more injections detectable. As you can see in figure 5, making Virgo around 10 times louder than the other detectors will increase the probability of a randomly localised injection to be detected. This is a controversial situation where we practically teach the model to ignore Virgo, unless the injection is really loud. It is not the first time [65] where HL analysis is better than HLV, assuming that our case of a loud Virgo resembles an HL analysis.

## IV. EVALUATION

With the investigation to find the best working model we found one with the best performance compared to others. The evaluation below describes how we calculated the values we talked in previous sections but focusing on the best current model for the final results.

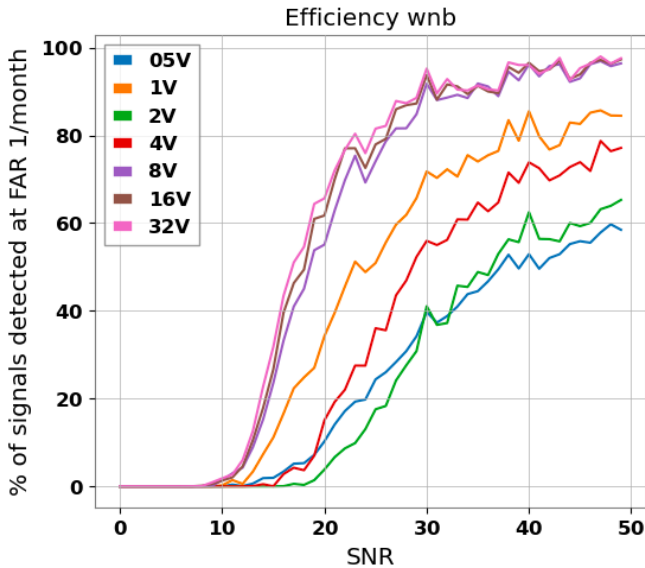


Figure 5: The average efficiency curve (out of 49 different combinations of model 1 and model 2) for WNB signals based on thresholds of 1/month of false alarm rates for each case, calculated from figure 4.

#### A. False Alarm Rate

A standard means to assess the performance of a GWB detection algorithm (see *e.g.* [48]) is to measure the detection efficiency for various signal morphologies as a function of the signal amplitude (*e.g.*, signal-to-noise ratio) at a fixed false alarm rate.

We calculate the false alarm rate (FAR) as a function of score by analysing background data samples that are independent from those used in the training. For the final model we measured the FAR using real LIGO-Virgo data from the second observing run during times when all three detectors were operating (1 - 25 Aug 2017), with time shifts applied as discussed in Section III B.

We consider that 1 per year for unmodelled searches is a good starting threshold to see if our models could be relevant for triggering electromagnetic follow-up observations. This choice is motivated by LIGO-Virgo for issuing public alerts of candidate signals[66]. Although we present the results of a calculated false alarm rate up to 10 years to show the limits of the current model.

From this distribution we can find our false alarm rate threshold (1/year) and calculate the detection efficiency. In figure 6 you see the false alarm rate for the currently best model found from the above investigation

#### B. Detection Efficiency

We calculate the detection efficiency of our model for a selection of different possible GWB signals, both for the case of simulated Gaussian background noise and for

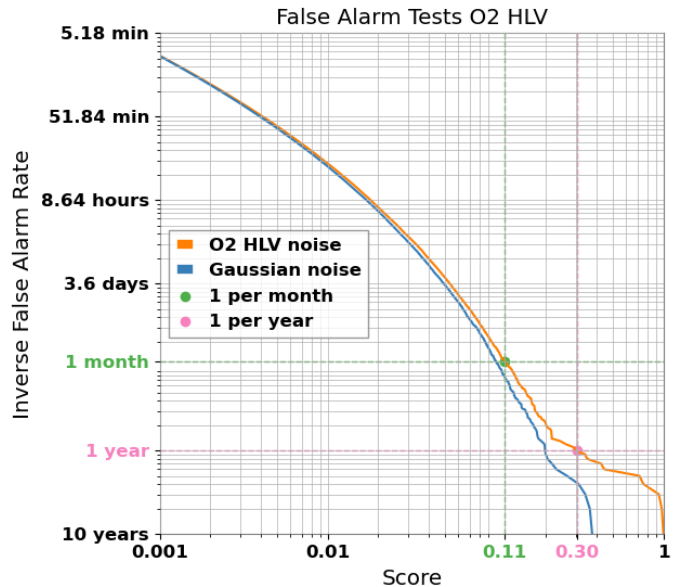


Figure 6: The false alarm rate on real O2 noise of the network in comparison with the false alarm rate of Gaussian noise. The score thresholds of 0.11 and 0.30 false alarm rates of 1/month and 1/year are also shown respectively.

real LIGO-Virgo data from the second observing run. In each case we generate new sets of signal injections (different from the training data) and add them on noise background randomly sampled from the O2 observing run during times when all three detectors were operating. We measure our sensitivity to five distinct waveform morphologies:

**WNB:** These are the same type of signal as the Type II used for training.

**CSG:** A circularly polarised sinusoidal signal with Gaussian envelope. These *ad hoc* waveforms are standard for testing GWB analyses [48, 49].

**CCSN:** The N20-2 waveform of [67], from a 3D simulation of a neutrino-driven core-collapse supernova (CCSN) explosion.

**Cusp:** The GW emission expected from cosmic string cusps [68].

**BBH:** The GW signal from a black-hole binary merger. We used the IMRPhenomD waveform model [69][70]. The black-hole masses and spins were selected randomly and uniformly over the intervals  $[10, 100] M_\odot$  and  $[-1, 1]$ , with the restriction that the signal maximum frequency had to stay below 512 Hz.

To create the efficiency curve we select a range of SNR values and for each one of those SNR values we generate

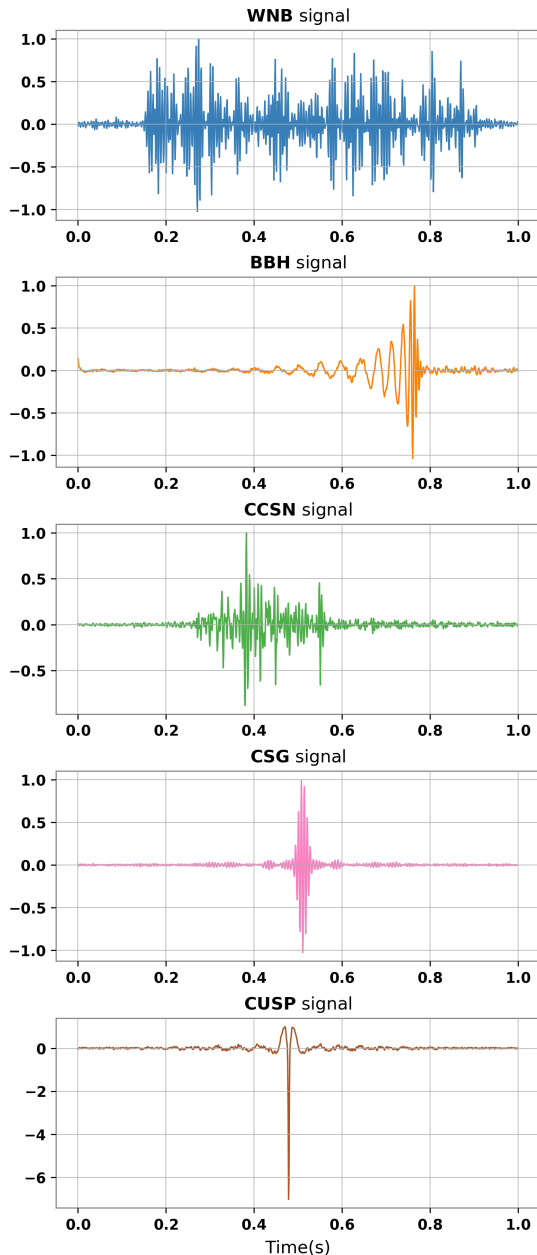


Figure 7: Examples of testing signals: white noise burst (WNB), binary black hole merger (BBH), core-collapse supernova (CCSN), circularly polarised sine-Gaussian (CSG) and cosmic string cusp.

$10^3$  injections (Type 2) where each one of them is re-scaled to match this value. Each injection is embedded to the background timeseries and it is processed by the models giving a score. The injection is considered to be detected if the output score is larger than that of the false alarm rate test threshold. We test those  $10^3$  signals of each morphology at each value of the range  $\rho = 0, 1, 2, \dots, 50$ , where the  $\rho = 0$  case corresponds to pure noise (expected zero efficiency).

Fig.8 shows the detection efficiency for each case. We see that we are able to detect  $>50\%$  ( $>90\%$ ) of all signals that have amplitudes  $\rho \geq 19$  ( $\rho \geq 27$ ), with the exception of cusps for which the sensitivity is lower. The performance for CCSN and BBH signals is very similar to that for WNBs, even though the signal morphologies are quite different. The performance for CSGs is even better, which we attribute to the very small time-frequency volume that it occupies making the signal louder. The performance for cusps is poorer, which probably occurs because cusps are linearly polarised and wnb training injections are elliptically polarised. This is also apparent in the difference in performance of SGE153Q8D9 and SGL153Q8D9 where a similar reduction of performance is detected for the linearly polarised signals. This is an interesting demonstration of where our training could potentially be improved to handle a yet broader range of signals.

We tested the models also on the five BBH signals that appear in August 2017 on the O2 run, but we didn't detect any of them. The non-detection of those BBH events is expected given their SNR values [3], which are lower than the calculated 50% threshold on BBH signals (19), shown in Figure 8.

### C. Comparison with all-sky search in O2

Except the performance test for the various waveforms above we do also a comparison of MLy with the all-sky search results for short duration burst in O2 observing run [71]. In this performance test we follow exactly the same procedure as before but instead we use the  $h_{rss}$  as a metric of intensity of the signal. Note here that the  $h_{rss}$  calculation happens before the whitening of the data. Hence signals with frequencies of low detector sensitivity will result to a reduced representation in SNR. There is no clear matching between SNR and  $h_{rss}$  due to that fact. The reason we use  $h_{rss}$  is because we need to have the same metric to compare the waveforms with other burst searches like O2 all-sky CWb search [49] results. In figure 9 we show the efficiency of some standard sub-second burst waveforms used to evaluate the performance of burst searches.

In Table I we show the comparison of the 50% efficiency thresholds of our search (iFAR 1 year) and cWB search (iFAR 100 years). Based on these results we cannot claim (and we do not) that the our pipeline is more sensitive than cWB in O2 HLV case, since  $h_{rss}$  thresh-

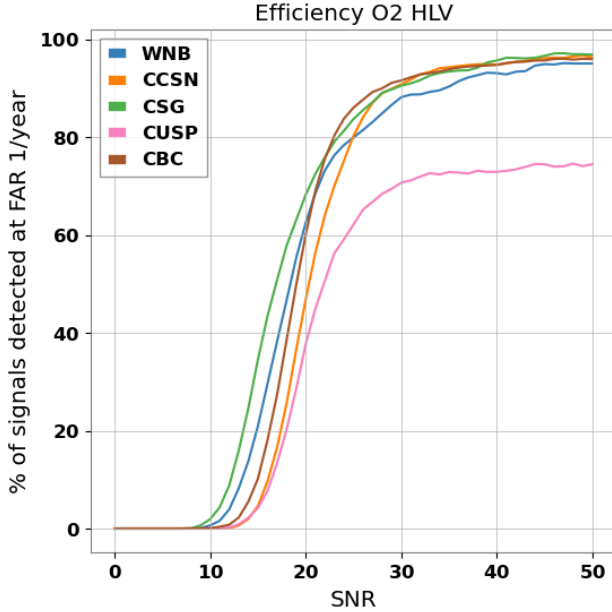


Figure 8: Detection efficiency : The fraction of simulated signals that are detected at a false alarm rate of 1 event per year versus the signal-to-noise ratio (SNR) defined by equation 3. The waveform morphologies are white noise burst (WNB), core-collapse supernova (CCSN), circularly polarised sine-Gaussian (CSG), cosmic string cusp, and binary black hole merger (BBH).

Performance comparison on the O2 HLV data set		
Morphology	cWB [49]	MLy
	$(10^{-22}\text{Hz}^{-1/2})$	$(10^{-22}\text{Hz}^{-1/2})$
Gaussian pulses		
$t=2.5$ ms	11	3.5
Sine-Gaussian wavelets		
$f_0=70$ Hz, $Q=3$	4.9	1.9
$f_0=153$ Hz, $Q=8.9$	1.4	1.7
$f_0=235$ Hz, $Q=100$	3.3	1.4
White-Noise Bursts		
$f_{low}=100$ Hz, $\Delta f=100$ Hz, $t=0.1$ s	1.4	1.7
$f_{low}=250$ Hz, $\Delta f=100$ Hz, $t=0.1$ s	1.4	1.8

Table I: The values shown refer to  $h_{rss}$ , in units of  $10^{-22}\text{Hz}^{-1/2}$ , at the 50% efficiency threshold. Comparing waveforms from cWB results [49] at FAR of 1 in 100 years and the MLy pipeline at false alarm of 1 per year. We restrict the comparison to injections with frequencies and durations that are in the range for which we have trained the MLy models (duration  $< 1$  s, frequencies in the 20 Hz - 480 Hz band).

olds are evaluated at different FARs. However we can

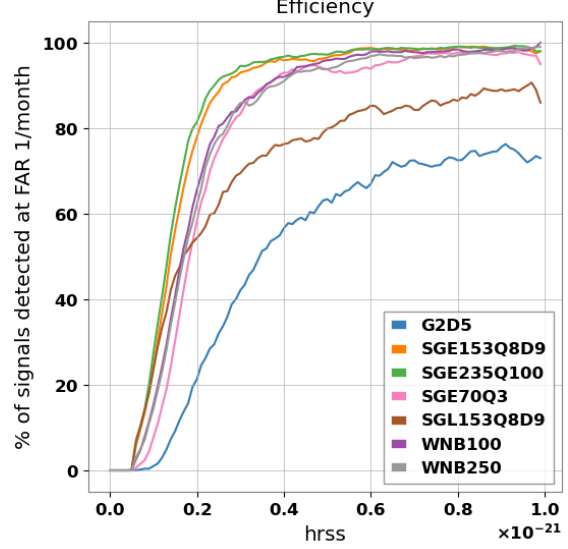


Figure 9: The detection efficiency of the MLy algorithm as a function of the  $h_{rss}$  for generic sub-second burst signals and for a false alarm rate of 1 per year, during the O2 HLV observing run.

see that out of almost all tested morphologies, any signal loud enough to be confidently detected by the cWB with  $\text{FAR} < 1/100$  years, would have shown up in the MLy search as a trigger loud enough to trigger an alert under the now-current alert threshold of  $\text{FAR} < 1/\text{year}$ . It is important to note that the G2D5 and SGL152Q8D9 injection sets were linearly polarised, while our training set consisted exclusively of unpolarised signals (WNBs with equal amplitudes in the two polarisations). We believe this to be the reason for MLy's poor limiting performance at high amplitudes for these injection sets. The same performance deficiency is observed also for the cases of Cusps which are also linearly polarised.

#### D. Inference Time

We note that the CNN analysis of data is very fast: we find that the average time required to process 1 second of data, given that the data are already downloaded and processed (without whitening included), is 51 ms on a 3.5 GHz Xeon E3-1240v5 quad-core CPU with 32 GB of RAM. This is much faster than the minute-scale latency typical of current LIGO-Virgo low-latency searches [17]. Also the time to train both models on a Tesla V100-SXM2-16GB GPU is  $\sim 12$  hours.i

Important to note is that due to the fact we train with artificial noise the training is independent of the observing run. A false alarm rate calculation would need to be repeated only to make sure that it stays stable along the run once in a while. By the time it is trained and tested,

inference the only thing we need to do.

Finally, given the low latency inference of those models, we suggest that it's combination with sky-localisation pipelines [72][22] can be a complete set for an unmodeled signal search. Although we understand that this needs more work to be generalised to unmodeled signals except CBCs.

## V. CONCLUSIONS

We have presented a novel CNN-based analysis pipeline for the detection of transient gravitational-wave signals. Unlike previous CNN-based analyses, our pipeline is capable of detecting waveforms with morphologies that are not included in the training set while rejecting real detector noise glitches. The analysis is shown to be sensitive to a variety of waveform morphologies at signal-to-noise ratios and false alarm rates relevant for issuing rapid alerts to the astronomical community, with very low latencies and computing requirements.

Our pipeline uses a multi-component architecture where one CNN detects transients that are simultaneous in multiple detectors while a second detects correlation between the detectors to eliminate coincident background glitches. The second CNN takes as input both the whitened detector timeseries data and the Pearson correlation between detectors computed for all physically allowed light travel time delays between detectors, allowing the CNN to detect signal correlation rather than signal shape. We suggest using separate models to identify different aspects or properties of the desired signal may be a useful approach generally for GW detection with machine learning methods.

While our model already has sensitivity approaching that of standard low-latency analyses, we consider this investigation to be a promising first attempt with potential for improvement. For example, training with more sophisticated simulated and real glitches may reduce the threshold required for the target false alarm rate, while training over a wider range of parameter space (like polarisations) may increase sensitivity to transients similar to cosmic string cusps.

---

[1] J. A. et al., *Classical and Quantum Gravity* **32**, 074001 (2015).

[2] F. A. et al., *Classical and Quantum Gravity* **32**, 024001 (2014).

[3] B. Abbott, R. Abbott, T. Abbott, *et al.* (LIGO Scientific Collaboration and Virgo Collaboration), *Physical Review X* **9** (2019), 10.1103/physrevx.9.031040.

[4] B. P. Abbott, R. Abbott, T. D. Abbott, *et al.* (LIGO Scientific Collaboration and Virgo Collaboration), *The Astrophysical Journal* **892**, L3 (2020).

[5] R. Abbott, T. Abbott, S. Abraham, *et al.* (LIGO Scientific Collaboration and Virgo Collaboration), *Physical Review D* **102** (2020), 10.1103/physrevd.102.043015.

[6] R. Abbott, T. D. Abbott, S. Abraham, *et al.*, *The Astrophysical Journal* **896**, L44 (2020).

[7] R. Abbott, T. D. Abbott, S. Abraham, *et al.* (LIGO Scientific Collaboration and Virgo Collaboration), *Phys. Rev. Lett.* **125**, 101102 (2020).

[8] <https://gracedb.ligo.org/superevents/public/O3/>.

[9] B. P. Abbott, R. Abbott, T. D. Abbott, *et al.* (LIGO Scientific Collaboration and Virgo Collaboration), *Phys. Rev. Lett.* **116**, 061102 (2016).

[10] B. P. Abbott, R. Abbott, T. D. Abbott, *et al.* (LIGO Scientific Collaboration and Virgo Collaboration), *The Astrophysical Journal Letters* **848:L12**, 59 (2017), arXiv:1710.05833 [astro-ph.HE].

[11] K. Kyutoku, S. Fujibayashi, K. Hayashi, K. Kawaguchi, K. Kiuchi, M. Shibata, and M. Tanaka, *Astrophys. J.* **890**, L4 (2020), arXiv:2001.04474 [astro-ph.HE].

[12] B. P. Abbott, R. Abbott, T. D. Abbott, *et al.* (LIGO Scientific Collaboration and Virgo Collaboration), *Phys. Rev. Lett.* **119**, 161101 (2017).

[13] D. Kasen, B. Metzger, J. Barnes, E. Quataert, and E. Ramirez-Ruiz, *Nature* **551**, 80 (2017).

[14] B. P. Abbott, R. Abbott, T. D. Abbott, *et al.* (LIGO Scientific Collaboration and Virgo Collaboration), *Phys. Rev. Lett.* **121**, 161101 (2018).

[15] B. P. Abbott, R. Abbott, T. D. Abbott, *et al.* (LIGO Scientific Collaboration and Virgo Collaboration), *The Astrophysical Journal* **850**, L39 (2017).

[16] B. P. Abbott, R. Abbott, T. D. Abbott, *et al.* (LIGO Scientific Collaboration and Virgo Collaboration), *Nature* **551**, 85 (2017).

[17] B. P. Abbott, R. Abbott, T. D. Abbott, *et al.* (LIGO Scientific Collaboration and Virgo Collaboration), *The Astrophysical Journal* **875**, 161 (2019).

[18] D. George and E. A. Huerta, *Physical Review D* **97**, 044039 (2017), arXiv: 1701.00008.

[19] H. Gabbard, M. Williams, F. Hayes, and C. Messenger, *Physical Review Letters* **120**, 141103 (2018), arXiv: 1712.06041.

[20] C. Bresten and J.-H. Jung, arXiv:1910.08245 [astro-ph, physics:gr-qc, physics:physics] (2019), arXiv: 1910.08245.

[21] H. Wang, Z. Cao, X. Liu, S. Wu, and J.-Y. Zhu, arXiv:1909.13442 [astro-ph, physics:gr-qc] (2019), arXiv: 1909.13442.

[22] C. Chatterjee, L. Wen, K. Vinsen, M. Kovalam, and A. Datta, *Physical Review D* **100** (2019), 10.1103/physrevd.100.103025.

[23] B. P. Abbott, R. Abbott, Abbott, and et al., *Physical Review Letters* **121** (2018), 10.1103/physrevlett.121.161101.

[24] J. W. Murphy, C. D. Ott, and A. Burrows, *The Astrophysical Journal* **707**, 1173 (2009).

[25] A. L. Piro and E. Pfahl, *The Astrophysical Journal* **658**, 1173 (2007).

[26] H. Shen, D. George, E. A. Huerta, and Z. Zhao, (2017), arXiv: 1711.09919.

[27] D. George and E. A. Huerta, arXiv:1711.07966 [astro-ph],

physics:gr-qc] (2017), arXiv: 1711.07966.

[28] A. Schmitt, K. Fu, S. Fan, and Y. Luo, in *Proceedings of the 2nd International Conference on Computer Science and Software Engineering*, CSSE 2019 (Association for Computing Machinery, New York, NY, USA, 2019) p. 73–78.

[29] T. D. Gebhard, N. Kilbertus, I. Harry, and B. Schölkopf, *Physical Review D* **100**, 063015 (2019), arXiv: 1904.08693.

[30] H.-M. Luo, W. Lin, Z.-C. Chen, and Q.-G. Huang, *Frontiers of Physics* **15**, 14601 (2019).

[31] X. Fan, J. Li, X. Li, Y. Zhong, and J. Cao, *Science China Physics, Mechanics & Astronomy* **62**, 969512 (2019).

[32] C. Chatterjee, L. Wen, F. Diakogiannis, and K. Vinsen, “Extraction of binary black hole gravitational wave signals from detector data using deep learning,” (2021), arXiv:2105.03073 [gr-qc].

[33] D. S. Deighan, S. E. Field, C. D. Capano, and G. Khanna, *Neural Computing and Applications* (2021), 10.1007/s00521-021-06024-4.

[34] H. Shen, E. A. Huerta, Z. Zhao, E. Jennings, and H. Sharma, arXiv:1903.01998 [astro-ph, physics:gr-qc, stat] (2019), arXiv: 1903.01998.

[35] W. Wei and E. Huerta, *Physics Letters B* **800**, 135081 (2020).

[36] S. B. Coughlin, S. Bahaadini, N. Rohani, M. Zevin, O. Patane, M. Harandi, C. Jackson, V. Noroozi, S. Allen, J. Areeda, M. W. Coughlin, P. Ruiz, C. P. L. Berry, K. Crowston, A. K. Katsaggelos, A. Lundgren, C. Osterlund, J. R. Smith, L. Trouille, and V. Kalogera, *Physical Review D* **99**, 082002 (2019), arXiv: 1903.04058.

[37] M. Razzano and E. Cuoco, *Classical and Quantum Gravity* **35**, 095016 (2018).

[38] P. Astone, P. Cerdá-Durán, I. Di Palma, M. Drago, F. Muciaccia, C. Palomba, and F. Ricci, *Phys. Rev. D* **98**, 122002 (2018).

[39] A. Iess, E. Cuoco, F. Morawski, and J. Powell, “Core-collapse supernova gravitational-wave search and deep learning classification,” (2020), arXiv:2001.00279 [gr-qc].

[40] J. Powell and B. Müller, *Monthly Notices of the Royal Astronomical Society* **487**, 1178 (2019).

[41] D. Radice, V. Morozova, A. Burrows, D. Vartanyan, and H. Nagakura, *The Astrophysical Journal Letters* **876**, L9 (2019).

[42] H. Andresen, E. Müller, H.-T. Janka, A. Summa, K. Gill, and M. Zanolin, *Monthly Notices of the Royal Astronomical Society* **486**, 2238 (2019).

[43] T. Takiwaki and K. Kotake, *Monthly Notices of the Royal Astronomical Society: Letters* **475**, L91 (2018).

[44] M. L. Chan, I. S. Heng, and C. Messenger, *Phys. Rev. D* **102**, 043022 (2020).

[45] M. López, I. Di Palma, M. Drago, P. Cerdá-Durán, and F. Ricci, *Phys. Rev. D* **103**, 063011 (2021).

[46] T. Marianer, D. Poznanski, and J. X. Prochaska, *Monthly Notices of the Royal Astronomical Society* **500**, 5408 (2020), <https://academic.oup.com/mnras/article-pdf/500/4/5408/34925881/staa3550.pdf>.

[47] S. Bahaadini, V. Noroozi, N. Rohani, S. Coughlin, M. Zevin, J. Smith, V. Kalogera, and A. Katsaggelos, *Information Sciences* **444**, 172 (2018).

[48] B. P. Abbott, R. Abbott, T. D. Abbott, *et al.* (LIGO Scientific Collaboration and Virgo Collaboration), *Phys. Rev. D* **95**, 042003 (2017).

[49] B. P. Abbott, R. Abbott, T. D. Abbott, *et al.* (LIGO Scientific Collaboration and Virgo Collaboration), *Phys. Rev. D* **100**, 024017 (2019).

[50] B. P. Abbott, R. Abbott, T. D. Abbott, *et al.* (LIGO Scientific Collaboration and Virgo Collaboration), *Classical and Quantum Gravity* **33**, 134001 (2016).

[51] S. Klimenko, G. Vedovato, V. Necula, F. Salemi, M. Drago, E. Chassande-Mottin, V. Tiwari, C. Lazzaro, B. O’Brian, M. Szczepanczyk, S. Tiwari, and V. Gayathri, (2020).

[52] R. Lynch, S. Vitale, R. Essick, E. Katsavounidis, and F. Robinet, *Phys. Rev. D* **95**, 104046 (2017).

[53] P. J. Sutton, G. Jones, S. Chatterji, P. Kalmus, I. Leonor, S. Poprocki, J. Rollins, A. Searle, L. Stein, M. Tinto, and M. Was, *New Journal of Physics* **12**, 053034 (2010).

[54] N. J. Cornish and T. B. Littenberg, *Classical and Quantum Gravity* **32**, 135012 (2015).

[55] H. Ismail Fawaz, G. Forestier, J. Weber, L. Idoumghar, and P.-A. Muller, *Data Mining and Knowledge Discovery* **33**, 917–963 (2019).

[56] L. N. Smith, “Cyclical learning rates for training neural networks,” (2017), arXiv:1506.01186 [cs.CV].

[57] B. P. Abbott, R. Abbott, T. D. Abbott, *et al.* (LIGO Scientific Collaboration and Virgo Collaboration and KAGRA Collaboration), *Living Rev Relativ* **21** (2013), arXiv:1304.0670 [gr-qc].

[58] LIGO Scientific Collaboration and Virgo Collaboration, “LIGO-Virgo strain data from observing run O2 (Nov 2016 - Aug 2017),” (2019).

[59] T. Damour and A. Vilenkin, *Phys. Rev. Lett.* **85**, 3761 (2000).

[60] V. Skliris, “MLy, gravitational waves and machine learning library,” <https://git.ligo.org/vasileios.skliris/mly>.

[61] A. Nitz, I. Harry, D. Brown, C. M. Biwer, J. Willis, T. D. Canton, *et al.*, “gwastro/pycbc: Pycbc release v1.16.9,” (2020).

[62] D. Macleod, A. L. Urban, S. Coughlin, T. Massinger, M. Pitkin, Rngeorge, Paulaltin, J. Areeda, L. Singer, E. Quintero, K. Leinweber, and T. G. Badger, “gwpv/gwpv: 2.0.1,” (2020).

[63] F. Chollet *et al.*, “Keras,” (2015).

[64] <https://git.ligo.org/vasileios.skliris/detecting-unmodeled-gravitational-wave-transients-using-convolutional-neural-networks>.

[65] T. L. S. Collaboration, the Virgo Collaboration, and the KAGRA Collaboration, “All-sky search for short gravitational-wave bursts in the third advanced ligo and advanced virgo run,” (2021), arXiv:2107.03701 [gr-qc].

[66] .

[67] Müller, E., Janka, H.-Th., and Wongwathanarat, A., *A&A* **537**, A63 (2012).

[68] T. Damour and A. Vilenkin, *Phys. Rev. D* **64**, 064008 (2001).

[69] S. Husa, S. Khan, M. Hannam, M. Pürrer, F. Ohme, X. J. Forteza, and A. Bohé, *Phys. Rev. D* **93**, 044006 (2016).

[70] S. Khan, S. Husa, M. Hannam, F. Ohme, M. Pürrer, X. J. Forteza, and A. Bohé, *Phys. Rev. D* **93**, 044007 (2016).

[71] B. Abbott, R. Abbott, T. Abbott, S. Abraham, F. Acernese, K. Ackley, C. Adams, R. Adhikari, V. Adya, C. Affeldt, and et al., *Physical Review D* **100** (2019), 10.1103/physrevd.100.024017.

[72] L. P. Singer and L. R. Price, *Physical Review D* **93**

(2016), 10.1103/physrevd.93.024013.